



Convective Heat Transfer Enhancement using Slot Jet Impingement on a Detached Rib Surface

A. K. Shukla and A. Dewan[†]

Department of Applied Mechanics, Indian Institute of Technology Delhi, New Delhi - 110016, India

[†]Corresponding Author Email: dewan_anupam@yahoo.com

(Received February 14, 2017; accepted July 9, 2017)

ABSTRACT

This paper presents results of a computational study to investigate the suitability of various RANS based turbulence models for slot jet impingement over flat and detached ribbed surfaces. The computed results are compared with the reported experimental data. It is observed that some turbulence models predict the experimental data with good trends, e.g., secondary peak in Nusselt number and distribution of normalized streamwise velocity. The standard $k-\omega$ and SST $k-\omega$ models predict heat transfer more accurately compared to that by other models with prediction of a secondary peak in Nusselt number. Distributions of turbulent kinetic energy, streamwise velocity and normal velocity are also analyzed to understand heat transfer behavior with flat and detached rib surfaces. Various parameters are considered to obtain a good understanding of heat transfer enhancement with jet impingement on a surface fitted with detached ribs. Further the effects of rib to plate clearance, position of first rib and Reynolds number on heat transfer characteristics are also investigated. It was observed that flow and heat transfer features are significantly affected by the placement of ribs on the impingement surface. Increasing the rib clearance, position of first rib in the streamwise direction and Reynolds number have favorable effects on heat transfer. The detached rib configuration offered augmentation in Nusselt number compared to the attached rib arrangement (i.e., with no clearance between the rib and impingement surface). Comparisons of stagnation point and average Nusselt numbers are also presented to understand heat transfer enhancement for flat and ribbed surfaces.

Keywords: Slot jet impingement; Heat transfer; Ribs; Turbulence modelling; Nusselt number; RANS.

NOMENCLATURE

B	slot width	P	mean pressure
c	rib clearance from impingement plate	p	rib pitch
c/B	non-dimensional rib clearance	p/e	non-dimensional rib pitch
e	rib height	Re	Reynolds number
e/B	non-dimensional rib height	T	mean temperature
H	height between jet to plate	U	mean velocity
H/B	non-dimensional nozzle to plate spacing	V_0	nozzle exit velocity
h	heat transfer coefficient	$x/B(R_1)$	position of first rib
k	thermal conductivity	x,y,z	coordinate directions
Nu	local Nusselt number	μ	dynamic viscosity
Nu_{av}	average Nusselt number		
Nu_{st}	stagnation point Nusselt number		

1. INTRODUCTION

Jet impingement on a heated plate is an interesting flow configuration to investigate because of its application in industry as well as fundamental importance. Jet impingement heat transfer on a solid flat surface has been a subject of wide interest both experimentally and computationally. Though jet

impingement on a flat or ribbed plate appears geometrically simple, it involves some interesting complex physical flow phenomena. Fig. 1 shows basic flow configurations involved with jet impingement, namely, free-shear region (here large scale vortex structures are formed), potential core, stagnation and wall jet regions. Modelling of flow separation and its reattachment can also be a

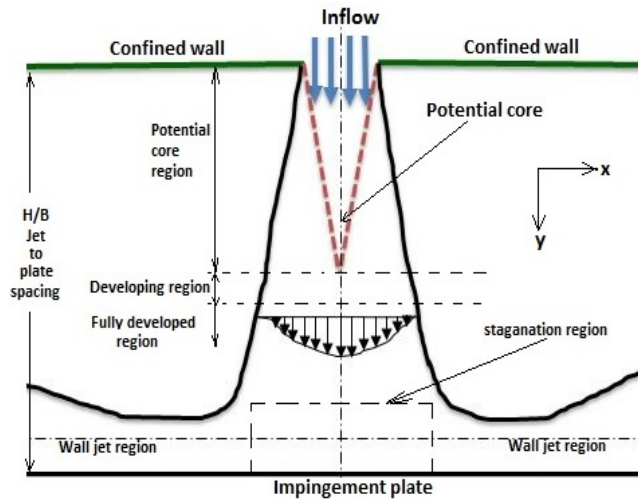


Fig. 1. Different regions of jet impingement flow.

challenging task with the presence of ribs on an impingement surface. Among all possible single phase heat transfer arrangements, jet impingement is claimed to have the maximum heat transfer rate (Dewan *et al.*, 2012). Some of its important industrial applications include cooling/ heating of electrical equipment or chips, internal cooling of turbine blades, cooling requirement in paper and textile industries, cooling of outer combustor walls, active cooling or heating in glass manufacturing industries, etc.

A free jet region will not exist if the jet exit is placed at a gap of two slot widths from the impingement surface (Ashforth-Frost *et al.*, 1997). Livingood and Hrycak (1973) investigated the length of the potential core region and it was observed to be nearly 4.7 to 7.7 times of slot width for slot jets. Two kinds of arrangements are possible for cooling of an impingement surface, i.e., jet impingement over a flat or a ribbed surface. In the present study jet impingement on attached and detached rib surfaces is considered. Some industrial applications of such configurations are cooling of electronic chips, internal passage cooling of turbine blade, etc.

A number of parameters have been identified in the literature that influence the flow and heat transfer features of an impinging jet, such as, jet to plate spacing, flow confinement, Reynolds number (Re), position of impingement surface, nozzle shape, jet inflow condition, etc. The effects of these parameters have been widely investigated experimentally and numerically (Ashforth-Frost and Jambunathan, 1996; Hoogendoorn, 1977; Ashforth-Frost *et al.*, 1997; Zhe and Modi, 2001; and Buchlin, 2011).

Many researchers (Cziesla *et al.*, 2001; Dairay *et al.*, 2014; and Dutta *et al.*, 2013b, 2016) noticed that large eddy simulation (LES) computations accurately predicted the flow and heat transfer features of impinging jets. But the LES computation of impinging jet is computationally quite expensive than its RANS modelling. Charmiyan *et al.* (2016) performed LES of water slot jet impingement with

H/B of 10 and $Re = 16000$. They considered two SGS models and observed that the predictions using the localized dynamic Smagorinsky model showed good agreement with the experimental results, especially in critical zones. For impinging flow computations with RANS modelling, use of appropriate wall functions is an important issue (Dewan *et al.*, 2012). Most of the RANS based turbulence models showed inaccuracy in computation of flow and heat transfer characteristics of an impinging jet upon comparison with experimental results, excluding some RANS models (Dutta *et al.*, 2013a and Behnia *et al.*, 1999). Al-Sanea S (1992) showed enhanced Nusselt number with Reynolds number and Prandtl number and it dropped with a contraction in the jet to plate spacing. Dutta *et al.* (2013a) observed that the Nusselt number profile for jet impingement over a flat surface was significantly influenced by the inflow turbulence intensity. They also observed that discretization scheme did not furnish any noteworthy change in their obtained results for Nusselt number.

Many authors, such as, Lytle and Webb (1994), Hoogendoorn (1977), Ashforth-Frost *et al.* (1997), Zhe and Modi (2001) and O'Donovan and Murray (2007), studied low nozzle to plate spacing. Lytle and Webb (1994), Ashforth-Frost *et al.* (1997) and O'Donovan and Murray (2007) observed secondary peak in the local Nu distribution for a low spacing (H/B). Hoogendoorn (1977) investigated the effect of small jet to plate spacing on Nu and observed slightly higher Nu values in the vicinity of the stagnation point. Lytle and Webb (1994) showed a significant enhancement in turbulence level and Nusselt number caused by accelerated impinging flow for low nozzle to plate spacing with an observation of inner and outer peaks in the distribution of local Nu . Ashforth-Frost *et al.* (1997) observed longer potential core length with the semi-confined jet impingement compared to that with an unconfined case. They observed this behavior due to scattering and narrow entrainment of jets. O'Donovan and Murray (2007) observed secondary peaks in the distribution of local Nusselt number in

radially outward direction for nozzle to impingement surface spacing less than two nozzle diameters due to a rapid increase in turbulence level in the region of wall jet. Zhe and Modi (2001) observed a clear secondary peak in shear at low value of jet to plate spacing and it vanished for a higher spacing. Ramesh *et al.* (2015, 2016) numerically investigated heat transfer problems with stretching sheet for variable thickness and convective boundary layer in the latter study. Krishnamurthy *et al.* (2016) investigated the effect of thermal radiation on melting heat transfer of nanofluid with nonlinear stretching sheet.

A very small number of studies have been reported either experimentally or numerically for slot jet impingement heat transfer over a ribbed surface. Various researchers have used ribbed surface in order to introduce flow unsteadiness and to enhance heat transfer rate (Muthukannan *et al.*, 2016; Katti and Prabhu, 2008; and Shukla and Dewan, 2016). For an impinging jet over a ribbed surface, the presence of ribs interrupts the wall jet and hence the turbulence level due to local roughness. As a result the local heat transfer is likely to increase (Zukerman and Lior, 2006). Katti and Prabhu (2008) noticed that an increment in the rib height resulted in a reduction of local heat transfer downstream of the first rib. Gau and Lee (1992) experimentally observed different flow and heat transfer features for impinging jet over a ribbed surface than that for a flat plate arrangement. They also observed a reduced stagnation heat transfer, i.e., close to the impingement region. Further Gau and Lee (2000) experimentally observed that with a highly turbulent impinging jet and hence turbulent wall jet a substantial augmentation in Nusselt number can be achieved. In a subsequent study, Gau and Lee (2000) considered jet impingement over a triangular ribbed surface. Recently Muthukannan *et al.* (2016) investigated flow and heat transfer features of a 2-D confined laminar slot jet impingement over a surface fitted with blocks. They observed a significant effect of blocks fitted on the impingement surface on heat transfer. Tan *et al.* (2014) experimentally observed nearly 30% enhanced heat transfer with the ribbed surface compared to a flat surface. They considered orthogonal, V and inverted V-shaped ribs configuration with jet to plate spacing (H/B) variation from 1 to 3 and Re from 6000 to 30000. Arquis *et al.* (2007) numerically observed an increased cooling performance of protruding blocks with jet Re and reduced channel height and slot width for multiple protruding heated blocks with laminar slot jet. Recently Shukla and Dewan (2017) reviewed various aspects of computational and experimental approaches for impinging jets. They concluded that there is a need for further investigation of application based jet impingement heat transfer configuration, including ribbed surface.

From the above-mentioned literature survey, it is clear that impinging jet heat transfer with ribbed surfaces has received less attention compared to that with flat surfaces. Two configurations of slot jet impingement are considered in the present study: jet impingement on (a) solid flat surface and (b) surface fitted with detached ribs. The objectives of the

present paper are to assess the performance of five turbulence models and check possible heat transfer enhancement with ribbed surfaces. For jet impinging on a surface fitted with detached ribs, governing parameters chosen to represent practical situations are the location of the first rib [$x/B(R_1)$] and clearance between rib and impingement surface (c/B). The rib width (w/B), rib height (e/B) and rib pitch (p/e) were kept constant for all the cases. For jet impingement on a surface fitted with detached ribs, values of parameters were chosen in such a way that interesting flow and heat transfer characteristics are meaningfully captured. Different values of Re were taken to assess its effect on flow and heat transfer features and to test possible heat transfer enhancement with ribbed surfaces.

2. COMPUTATIONAL DOMAIN, GRID AND METHODOLOGY

All the computations were performed using an unstructured and cell-centered finite-volume code ANSYS FLUENT 15, which employs a co-located grid arrangement. The second-order central difference and upwind schemes were used for discretization of the diffusive and convective terms of the governing equation, respectively. The SIMPLE algorithm was used for the pressure-velocity coupling. Fig. 2 shows the computational domain, boundary condition and grid distribution used in the present study. The origin of the coordinate system was located at the impingement plate on the jet centerline (Fig. 2). The no slip wall boundary condition was used at all the solid walls, such as, confined wall, ribs wall and impingement wall. A constant heat flux of 4000 W/m^2 was applied at the impingement plate. Heat losses due to radiation, viscous dissipation and body forces were neglected. A fully developed condition at the jet exit was considered. The jet exit velocity (V_0) based on the jet Re , turbulence intensity (I) of 1% and turbulent length scale of $0.015B$ were specified at the jet inlet. The outflow boundary conditions were specified at the outlet on the either side of the jet located at an adequately large distance i.e., at $x/B = \pm 60B$ to avoid flow reversal. Grids were made denser at critical sectors, such as, close to the ribbed surface, impingement surface and in rib to plate clearances in order to achieve a reasonable compromise in computational accuracy and cost.

The Reynolds-averaged Navier-Stokes (RANS) computations were performed, which involves solutions of the time-averaged governing equations. In this approach, the instantaneous velocity field may be divided into its time-averaged $\bar{u}_i(x)$ (mean) and fluctuating parts $u'_i(x, t)$, in such a way that $\bar{u}'_i = 0$. The time-averaged Navier-Stokes equations result in extra terms, known as the Reynolds stresses. Similarly the time-averaging of the energy equation results in extra terms known as the turbulent heat flux. These additional terms need to be modelled in order to close the system of equations. The time-averaged governing equations for the conservations of mass, momentum and energy may be written as

$$\frac{\partial \rho}{\partial t} + \rho \frac{\partial \bar{u}_i}{\partial x_i} = 0 \quad (1)$$

$$\frac{\partial \bar{u}_i}{\partial t} + \bar{u}_j \frac{\partial \bar{u}_i}{\partial x_j} = -\frac{1}{\rho} \frac{\partial \bar{p}}{\partial x_i} + \frac{1}{\rho} \frac{\partial}{\partial x_j} (2\mu \bar{S}_{ij} - \rho \overline{u'_i u'_j}) \quad (2)$$

$$\frac{\partial \bar{T}}{\partial t} + \bar{u}_j \frac{\partial \bar{T}}{\partial x_j} = \frac{1}{\rho} \frac{\partial}{\partial x_j} \left(\frac{\kappa}{c_p} \frac{\partial \bar{T}}{\partial x_j} - \rho \overline{u'_i T'} \right) \quad (3)$$

where,

$$\bar{S}_{ij} = \frac{1}{2} \left(\frac{\partial \bar{u}_i}{\partial x_j} + \frac{\partial \bar{u}_j}{\partial x_i} \right)$$

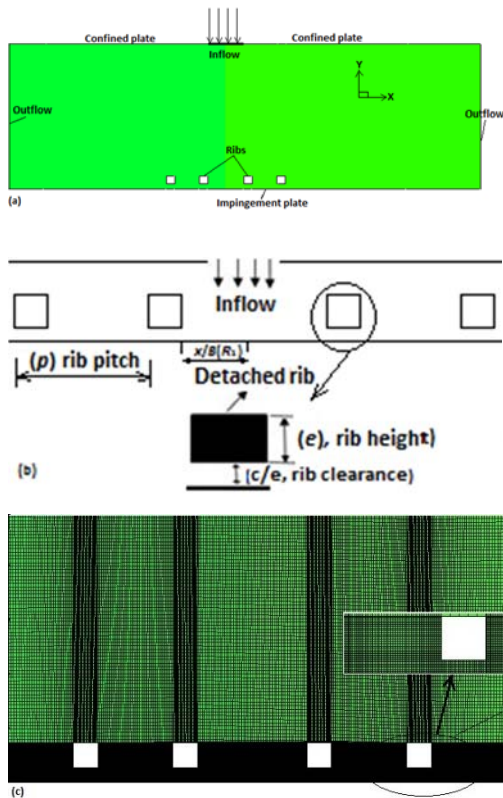


Fig. 2. Computational domain and grid used.

The eddy viscosity hypothesis (Boussinesq approximation) relates the Reynolds stresses to the mean velocity gradients as

$$-\rho \overline{u'_i u'_j} = 2\mu_t \bar{S}_{ij} - \frac{2}{3} \rho k \delta_{ij} \quad (4)$$

here k is the turbulent kinetic energy defined as $k = \frac{1}{2} \overline{u'_i u'_i}$, δ_{ij} denotes the Kronecker delta ($\delta_{ij} = 1$ if $i = j$ and $\delta_{ij} = 0$ if $i \neq j$) and μ_t is the turbulent or eddy viscosity.

The turbulent heat or scalar flux can be modelled in the same way as Reynolds stresses and can be written as

$$-\rho \overline{u'_i T'} = \frac{\mu_t}{Pr_t} \frac{\partial \bar{T}}{\partial x_i} \quad (5)$$

The turbulent Prandtl number (Pr_t) is specified as the

ratio of the eddy viscosity (μ_t) to the eddy thermal diffusivity (Γ) i.e., $Pr_t = \frac{\mu_t}{\Gamma}$.

2.1 k - ϵ Based Turbulence Models

These are two-equation models in which the evolution equations of turbulent kinetic energy (k) and dissipation rate (ϵ) are solved and the eddy viscosity is specified using k and ϵ . In this model, the ϵ equation contains a term that cannot be calculated at a wall (Dewan, 2011). Therefore, suitable wall functions need to be used with this model. In the present paper, the standard k - ϵ , RNG k - ϵ and realizable k - ϵ models were used for computations along with enhanced wall treatment.

2.1.1 Standard k - ϵ Model

It is a two-equation semi-empirical model (Launder and Spalding, 1974) and perhaps the most robust, economical and widely used turbulence model. This model works well only for fully turbulent flows and requires wall functions for computations in the vicinity of a wall. The eddy viscosity is modelled as

$$\mu_t = \rho C_\mu \frac{k^2}{\epsilon} \quad (6)$$

where C_μ is an empirical constant. The modelled transport equations for k and ϵ may be written as

$$\begin{aligned} \frac{\partial}{\partial t} (\rho k) + \frac{\partial}{\partial x_i} (\rho k \bar{u}_i) &= \frac{\partial}{\partial x_j} \left[\left(\mu + \frac{\mu_t}{\sigma_k} \right) \frac{\partial k}{\partial x_j} \right] + P_k - \rho \epsilon \end{aligned} \quad (7)$$

$$\begin{aligned} \frac{\partial}{\partial t} (\rho \epsilon) + \frac{\partial}{\partial x_i} (\rho \epsilon \bar{u}_i) &= \frac{\partial}{\partial x_j} \left[\left(\mu + \frac{\mu_t}{\sigma_\epsilon} \right) \frac{\partial \epsilon}{\partial x_j} \right] \\ &+ C_{1\epsilon} \frac{\epsilon}{k} P_k - C_{2\epsilon} \rho \frac{\epsilon^2}{k} \end{aligned} \quad (8)$$

where the term P_k in Eq. (7) denotes the production of turbulent kinetic energy and is modelled as

$$P_k = \mu_t \bar{S}^2$$

The magnitude of the time-averaged strain rate tensor (\bar{S}) is given as

$$\bar{S} = \sqrt{2 \bar{S}_{ij} \bar{S}_{ij}}$$

The values of model constants (Dewan, 2011) are $C_{1\epsilon} = 1.44$, $C_{2\epsilon} = 1.92$, $C_\mu = 0.09$, $\sigma_k = 1$ and $\sigma_\epsilon = 1.3$.

2.1.2 RNG k - ϵ Model

This model is a slightly modified form of the standard k - ϵ model. It is derived using the renormalization group theory (Yakhot and Orszag, 1986). It is known to work better than the standard k - ϵ model in some complex shear flows, e.g., flows with high swirl, strain rates and separation. This model provides good estimate of the spread rates of slot and round jets. A modified equation for

dissipation is employed in this model. The corresponding governing equations may be written as

$$\frac{\partial}{\partial t}(\rho k) + \frac{\partial}{\partial x_i}(\rho k \bar{u}_i) = \frac{\partial}{\partial x_j} \left[\left(\mu + \frac{\mu_t}{\sigma_k} \right) \frac{\partial k}{\partial x_j} \right] + P_k - \rho \varepsilon \quad (9)$$

$$\frac{\partial}{\partial t}(\rho \varepsilon) + \frac{\partial}{\partial x_i}(\rho \varepsilon \bar{u}_i) = \frac{\partial}{\partial x_j} \left[\left(\mu + \frac{\mu_t}{\sigma_\varepsilon} \right) \frac{\partial \varepsilon}{\partial x_j} \right] + C_{1\varepsilon} \frac{\varepsilon}{k} P_k - C_{2\varepsilon}^* \rho \frac{\varepsilon^2}{k} \quad (10)$$

with

$$C_{2\varepsilon}^* = C_{2\varepsilon} + \frac{C_\mu \eta^3 (1 - \frac{\eta}{\eta_0})}{1 + \beta \eta^3}$$

where

$$\eta = \frac{Sk}{\varepsilon}$$

The model constants (Dewan, 2011) are $C_{1\varepsilon} = 1.42, C_{2\varepsilon} = 1.68, \eta_0 = 4.38, \beta = 0.012, \sigma_k = 0.7194$ and $\sigma_\varepsilon = 0.7194$.

2.1.3 Realizable $k-\varepsilon$ Model

In this model, a variable C_μ based on the positivity of the normal stresses and Schwarz inequality for shear stresses is used. Further, the dissipation rate equation is modified based on the equation for the mean-square vorticity fluctuations (Shih *et al.*, 1995). The corresponding governing equations may be written as

$$\frac{\partial}{\partial t}(\rho k) + \frac{\partial}{\partial x_i}(\rho k \bar{u}_i) = \frac{\partial}{\partial x_j} \left[\left(\mu + \frac{\mu_t}{\sigma_k} \right) \frac{\partial k}{\partial x_j} \right] + P_k - \rho \varepsilon \quad (11)$$

$$\frac{\partial}{\partial t}(\rho \varepsilon) + \frac{\partial}{\partial x_i}(\rho \varepsilon \bar{u}_i) = \frac{\partial}{\partial x_j} \left[\left(\mu + \frac{\mu_t}{\sigma_\varepsilon} \right) \frac{\partial \varepsilon}{\partial x_j} \right] + \rho C_1 S \varepsilon - \rho C_2 \frac{\varepsilon^2}{k + \sqrt{\vartheta} \varepsilon} \quad (12)$$

where, $C_1 = \max[0.43, \frac{\eta}{\eta+5}]$. The variable C_μ in the definition of the eddy viscosity is given by the expression

$$C_\mu = \frac{1}{A_0 + A_s \frac{kU^*}{\varepsilon}}$$

where, $U^* = \sqrt{S_{ij}S_{ij} + \bar{\Omega}_{ij}\bar{\Omega}_{ij}}$, $\bar{\Omega}_{ij} = \Omega_{ij} - 2\varepsilon_{ijk}\omega_k$

with $A_0 = 4.04$ and $A_s = \sqrt{6} \cos \phi$

$$\phi = \frac{1}{3} \cos^{-1}(\sqrt{6}W), W = \frac{S_{ij}S_{jk}S_{ki}}{S^3} \tilde{S} = \sqrt{S_{ij}S_{ij}}$$

The model constants (Dewan, 2011) are $C_2 = 1.9$, $\sigma_k = 1$ and $\sigma_\varepsilon = 1.2$.

2.1.4 Enhanced Wall Treatment

It is a near wall modelling technique used along with different variants of the standard $k-\varepsilon$ turbulence model. It uses a two-layer model and hence it is also termed as the two-layer methodology for wall treatments. This type of wall treatment is appropriate for complex and low- Re flows. Usually a fine mesh is used close to the wall (typically $y^+ \approx 1$) which should be capable of resolving the viscous sub-layer. A combination of two-layer model is used to compute the dissipation field close to a wall. The flow domain is divided in two regions, i.e., viscosity affected or viscous sub-layer region and outer region (fully turbulent region). It is implemented based on turbulent Reynolds number (which demarcates the two regions based on the normal wall distance) which is defined as

$$Re_y = \frac{\rho y \sqrt{k}}{\mu}$$

where y denotes the wall normal distance and k turbulent kinetic energy. For $Re_y < 200$ (viscosity affected region) the one-equation model of Wolfstein (1969) is used and for $Re_y > 200$ (turbulent affected region) the $k-\varepsilon$ models are used. With enhanced wall functions a blended law of the wall is used in the momentum boundary condition (proposed by Kedar, 1981)

$$u^+ = e^\Gamma u_{lam}^+ + u_{tur}^+ e^{1/\Gamma}$$

Here the blending function Γ is given as

$$\Gamma = -\frac{a(y^+)^4}{1 + by^+}$$

here $a = 0.01$ and $b = 5$. The enhanced thermal wall functions (T^+) are similar to those used for u^+ .

2.2 $k-\omega$ Based Turbulence Models

In this group of models, transport equations for turbulent kinetic energy (k) and specific dissipation rate ($\omega = \frac{\varepsilon}{k}$) are solved to specify the turbulent viscosity. In the present study, two versions of the $k-\omega$ model were considered, namely, the standard $k-\omega$ model and the SST $k-\omega$ model.

2.2.1 Standard $k-\omega$ Model

The modelled equations for k and ω do not comprise any terms that are undefined at the wall, i.e., the model may be used without wall functions. It performs well in case of separated flows and flows with pressure gradient. The transport equations for k and ω may be written as (Wilcox, 2006)

$$\frac{\partial}{\partial t}(\rho k) + \frac{\partial}{\partial x_i}(\rho k \bar{u}_i) = \frac{\partial}{\partial x_j} \left[\left(\mu + \frac{\mu_t}{\sigma_k} \right) \frac{\partial k}{\partial x_j} \right] + P_k - \rho \beta^* f_\beta k \omega \quad (13)$$

$$\frac{\partial}{\partial t}(\rho \omega) + \frac{\partial}{\partial x_i}(\rho \omega \bar{u}_i) = \frac{\partial}{\partial x_j} \left[\left(\mu + \frac{\mu_t}{\sigma_\omega} \right) \frac{\partial \omega}{\partial x_j} \right] + \alpha \frac{\omega}{k} P_k - \rho \beta f_\beta \omega^2 \quad (14)$$

where,

$$f_{\beta^*} = \begin{cases} 1 & x_k \leq 0 \\ \frac{1 + 680x_k^2}{1 + 400x_k^2} & x_k > 0 \end{cases}$$

$$x_k = \frac{1}{\omega^3} \frac{\partial k}{\partial x_j} \frac{\partial \omega}{\partial x_j}$$

$$f_{\beta} = \frac{1 + 70x_{\omega}}{1 + 80x_{\omega}}$$

$$x_{\omega} = \left| \frac{\Omega_{ij} \Omega_{jk} S_{ki}}{(\beta_{\infty}^* \omega)^3} \right|$$

The turbulent viscosity is modelled as

$$\mu_t = \alpha^* \rho \frac{k}{\omega}$$

The values of the model constants for the standard $k-\omega$ model are $\alpha_{\infty}^* = 1$, $\alpha_{\infty} = 0.52$, $\alpha_0 = \frac{1}{9}$, $\beta_{\infty}^* = 0.09$, $\beta_i = 0.072$, $\alpha^* = \alpha_{\infty}^*$, $\alpha = \alpha_{\infty}$, $\sigma_k = 2$ and $\sigma_{\omega} = 2$ (Dewan, 2011).

2.2.2 SST $k-\omega$ model

Menter (1994) proposed this model based on the blending of the standard $k-\omega$ model near the wall to a transformed $k-\epsilon$ model away from the wall, i.e., in the free-stream region. Here a cross-diffusion term in the ω equation was also introduced. Further, the definition of the eddy viscosity changes from that of the standard $k-\omega$ model and is given as

$$\mu_t = \rho \frac{k}{\omega} \frac{1}{\max\left[\frac{1}{\alpha^*}, \frac{SF_2}{a_1 \omega}\right]}$$

The transport equations for k and ω are

$$\begin{aligned} & \frac{\partial}{\partial t}(\rho k) + \frac{\partial}{\partial x_i}(\rho k \bar{u}_i) \\ & = \frac{\partial}{\partial x_j} \left[\left(\mu + \frac{\mu_t}{\sigma_k} \right) \frac{\partial k}{\partial x_j} \right] \\ & + \min(P_k, 10\rho\beta^*k\omega) - \rho\beta^*k\omega \end{aligned} \quad (15)$$

$$\begin{aligned} & \frac{\partial}{\partial t}(\rho\omega) + \frac{\partial}{\partial x_i}(\rho\omega \bar{u}_i) \\ & = \frac{\partial}{\partial x_j} \left[\left(\mu + \frac{\mu_t}{\sigma_{\omega}} \right) \frac{\partial \omega}{\partial x_j} \right] + \alpha \frac{\omega}{k} P_k - \rho\beta\omega^2 + 2 \left(1 - F_1 \right) \frac{\rho\sigma_{\omega 2}}{\omega} \frac{\partial k}{\partial x_j} \frac{\partial \omega}{\partial x_j} \end{aligned} \quad (16)$$

The last term in Eq. (16) is called the cross-diffusion term. Here various coefficients in the SST $k-\omega$ model are characterized by means of the blending functions F_1 and F_2 .

$$\sigma_k = \frac{1}{F_1/\sigma_{k,1} + (1 - F_1)/\sigma_{k,2}}$$

$$\sigma_{\omega} = \frac{1}{F_1/\sigma_{\omega,1} + (1 - F_1)/\sigma_{\omega,2}}$$

$$\alpha_{\infty} = F_1\alpha_{\infty,1} + (1 - F_1)\alpha_{\infty,2}$$

here σ_k and σ_{ω} denote turbulent Prandtl numbers for k and ω , respectively.

Three additional parameters considered in the present study, namely, the Reynolds number (Re), local Nusselt number (Nu) and average Nusselt number (Nu_{av}) are defined as

$$Re = \frac{\rho UB}{\mu}$$

$$Nu = \frac{h_x B}{k_a}$$

where

$$h_x = \frac{q_w}{T_w - T_f}$$

The average Nusselt number (Nu_{av}) is given by the expression

$$Nu_{av} = \frac{1}{A} \int Nu_x dA$$

Here h_x denotes the local heat transfer coefficient, k_a the thermal conductivity of air and B the slot width. T_w and T_f are the temperatures of the wall and fluid, respectively. Other symbols used here carry their standard meanings.

3. RESULTS AND DISCUSSION

Two configurations were considered in the present study. In the first case the jet impinging on a solid flat surface and in second case the jet impinged on a surface fitted with ribs. We have considered $H/B = 4$ for both the cases with several values of Re based on the inlet velocity and slot width (B). For jet impinging on a ribbed surface two ribs on either side of the centerline of the jet were considered. Performance of five RANS turbulence models, namely, the standard $k-\epsilon$, RNG $k-\epsilon$, realizable $k-\epsilon$, SST $k-\omega$ and standard $k-\omega$ models were assessed in order to check their applicability for such complex flow configurations. For jet impinging on a surface fitted with two detached ribs placed in the wall jet region, governing parameters chosen to represent practical situations, namely, the non-dimensional location of the first rib [$x/B(R_1)$] equal to 0.5 and 1, non-dimensional clearance between rib and wall (c/B) equal to 0, 0.067, 0.134 and 0.201, the non-dimensional rib width and height (w/B and e/B) equal to 0.023, i.e., square cross section ribs. The rib pitch (p/e) equal to 4 was kept constant in all the cases. Various values of Re were used to check its effect on the local heat transfer. A detailed comparison of local and average Nusselt numbers has been presented to understand heat transfer enhancement. Table 1 shows different jet impingement configurations and parameters used in the present study.

Table 1 Various configurations considered

S. No.	Configurations	Parameters studied	Re
1.	Flat surface	$H/B = 4$	20000
2.	Detached rib	$H/B = 4, p/e = 4, c/B = 0, 0.067, 0.134$ and 0.201, $x/B(R_1) = 0.5$ and 1.	5500, 10000, 15000 and 20000

The present code was validated with the available experimental (Ashforth-Frost *et al.*, 1997) and computational (Dutta *et al.*, 2013a) results for jet impingement on a flat surface with $H/B = 4$ and $Re = 20000$. Comparisons of the normalized mean streamwise velocity and Nusselt number (Nu) variations are presented for the code validation. Fig. 3 (a, b) shows the mean velocity profiles using five turbulence models for $H/B = 4$ and $Re = 20000$ at $x/B = 1$ and 2 close to the impingement plate, stagnation and wall jet regions. Fig. 3 (a, b) shows that the present mean streamwise velocity profiles at $x/B = 1$ and 2 follow the same trend as in the reported data. Here all the computations (present as well as the reported in the literature) over-predict the variation of the mean velocity along y/B at $x/B = 1$ [Fig. 3(a)]. This over-prediction of the mean velocity in the stagnation region is due to the over-prediction of the stagnation zone by the RANS based turbulence models in general. It can be observed that $U/V_0 = 0.73$ between $y/B = 0.05 - 0.35$ and thereafter it increases at higher y/B values. This behavior is due to the influence of vertical velocity component. From Fig. 3 (b) it can be noticed that the present predictions of the normalized streamwise velocity are in good agreement with the reported experimental and computational data. It can also be observed that except the standard $k-\epsilon$ model, which under-predicts the distribution of streamwise velocity, all other models show good agreement at $x/B = 1$ and 2 [Figs. 3(a) and 3(b)].

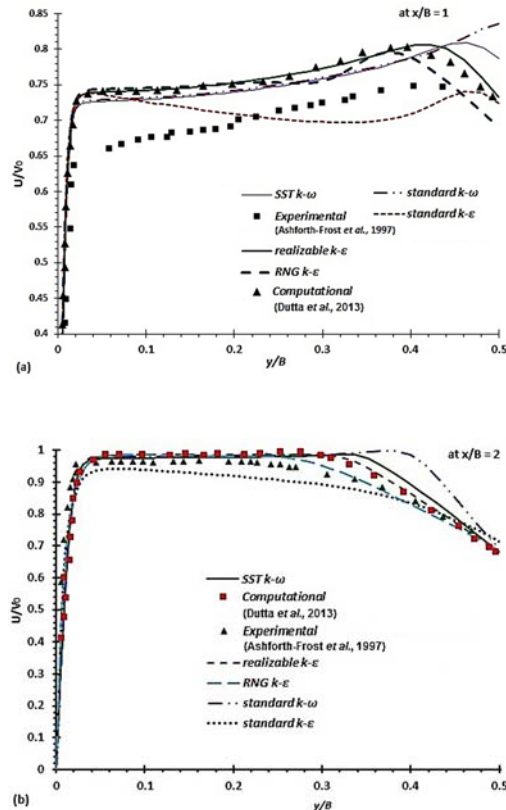


Fig. 3. Streamwise mean velocity profiles using different turbulence models for $H/B = 4$ and $Re=20000$ at (a) $x/B = 1$ and (b) $x/B = 2$.

The present computations were also compared with the experimental data of Ashforth-Frost *et al.* (1997) (Fig. 4) for the local Nusselt number (Nu). The present results follow the same trend as those of Ashforth-Frost *et al.* (1997). As expected, a secondary peak in the Nu over the impingement plate in the stream-wise direction can be observed (Fig. 4). The present predictions of the surface Nu show a dip approximately at the same location as in the experimental observations (Fig. 4). However, in the region of the secondary peak the surface Nusselt number is over-predicted, probably because of several assumptions involved with the turbulence models considered. The standard and SST $k-\omega$ turbulence models are able to predict the secondary peak in Nusselt number (Fig. 4). It is well known that the occurrence of the secondary peak in Nu is due to laminar to turbulent transition in the wall jet region (Ashforth-Frost *et al.*, 1997). The SST $k-\omega$ turbulence model (Menter, 1994) is known to work well under adverse pressure gradients and separating flow situations.

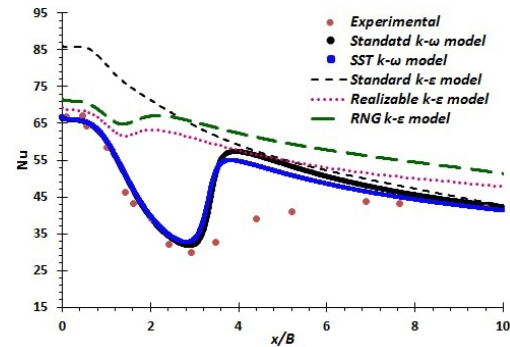


Fig. 4. Local Nu distributions using different turbulence models for $H/B = 4$ and $Re = 20000$.

It can also be observed from Fig. 4 that the standard $k-\epsilon$ model highly over-predicts the stagnation point Nu as well as variation of the surface Nusselt number. Further it does not predict the secondary peak in Nu . The standard $k-\epsilon$ model is known to perform poorly for flows with strong separation and large streamline curvature (Dewan, 2011). However, the present results with the realizable and RNG $k-\epsilon$ models show a slight secondary peak in Nu but its location and values deviate from the experimental results (Fig. 4). Thus all three variants of the $k-\epsilon$ model were found to be unsuitable due to their inability to capture transition. A good prediction of transition is highly desirable in the case of low nozzle to plate spacing. Therefore, we have used the SST $k-\omega$ turbulence model for all the cases with $H/B = 4$. It is quite important to maintain y^+ value at the first grid points in the vicinity of a wall to less than one in order to capture laminar and transitional boundary-layers. In the present study we ensured that the y^+ values were maintained approximately in the range of 1 - 2 in all computations.

Profiles of TKE (k) at different x/B locations and in the vicinity of the impingement plate are shown in Fig. 5. An augmentation in TKE near the location of

the secondary peak in Nu , i.e., at $x/B = 3.5, 4$ and 5 can be observed (Fig. 5). A secondary peak in Nu (Fig. 4) can be associated with an augmentation in TKE in the region of the secondary peak. Fig. 6 shows the contours of turbulent kinetic energy (TKE) for flat plate at $H/B = 4$ and $Re = 20000$ with SST $k-\omega$ and standard $k-\epsilon$ turbulence models. It can be observed here that the contours of TKE show a higher value in the stagnation region with the standard $k-\epsilon$ model compared to the SST $k-\omega$ model. Due to a higher value of TKE in the stagnation region the standard $k-\epsilon$ model overpredicts the value of the stagnation point Nu (Fig. 4).

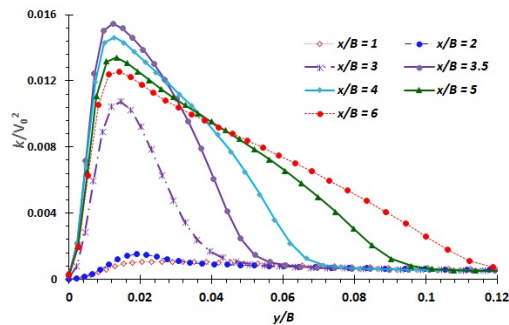


Fig. 5. Profiles of TKE (k) at different x/B locations along y/B for flat plate at $H/B = 4$.

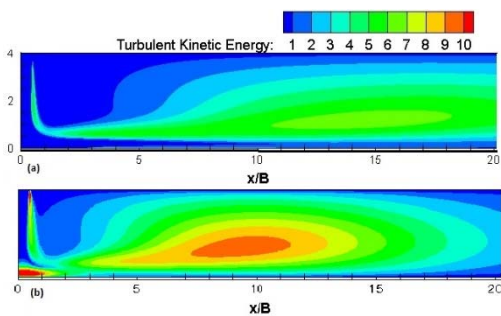


Fig. 6. Contours of TKE for flat plate at $H/B=4$ with (a) SST $k-\omega$ model and (b) standard $k-\epsilon$ turbulence model.

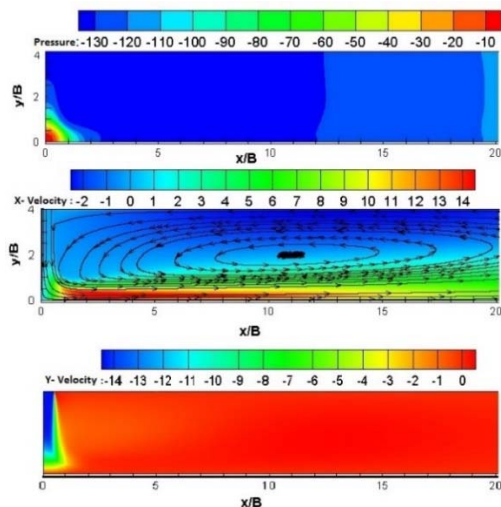


Fig. 7. Contours of (a) pressure, (b) streamwise velocity and (c) normal velocity for flat plate at $H/B = 4$.

Fig. 7 shows contours of pressure, x and y -velocities for $H/B = 4$ at $Re = 20000$. The stagnation point (at $x/B = 0$) can be clearly observed (Fig. 7). It can be further observed that the impingement plate was kept inside the potential core [Fig. 7(c)]. Flow deflection in the stagnation and wall jet regions in the x -direction with sharp decelerated flow followed by flow acceleration in the x -direction can be observed (Fig. 7). Fig. 8 shows distribution of the normalized mean streamwise velocity at different x/B locations near the impingement surface. From Fig. 8 it can be observed that at $x/B = 2 - 3$ the wall velocity peaks, i.e., $u/V_0 = 0.995$ and at this x/B value a local minima in the surface Nusselt number can be observed (Fig. 4). However, due to an over-prediction of the stagnation zone with the RANS based models the mean velocities are slightly over-predicted at higher x/B values as the velocity is expected to decrease in magnitude due to the wall jet spread.

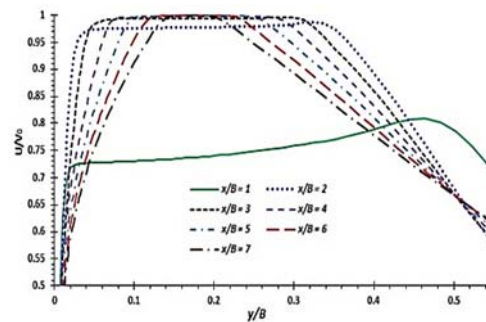


Fig. 8. Streamwise mean velocity distributions for $H/B = 4$ and $Re = 20000$ at different x/B locations.

In the present study, various parameters were considered to obtain a good understanding of enhancement in heat transfer with jet impingement on a surface with detached ribs mounted on it. Two ribs in the streamwise direction on either side of the centerline of the slot jet were considered. Here we have assessed the effect of the rib clearance (c/B), position of first rib [x/B (R_1)] and Re on heat transfer characteristics. We have observed that flow and heat transfer characteristics are greatly affected by the placement of ribs on impingement surface.

For grid independence study we have used grids with number of cells equal to 260125, 425312, 476235 and 567425 and compared variation of local Nusselt number in the streamwise direction (Fig. 9). The local Nu distributions using two fine meshes are almost grid independent (Fig. 9).

Figure 10 shows a comparison of the local Nu for flat plate and detached ribs (for $c/B = 0.067$ and 0.134) with $H/B = 4$ and $Re = 20000$ using the SST $k-\omega$ turbulence model. It can be observed that the local Nu is more with detached rib compared to that for flat plate, except in the stagnation region and between ribs (Fig. 10). The effect of the rib clearance on the local Nu is also compared in Fig. 10 and it can

be observed here that an increment in the rib clearance has an advantageous effect on the local heat transfer as well as the stagnation point Nusselt number. Local Nu is seen to increase under the rib (Fig. 10) and this behavior may be attributed to flow acceleration taking place under the detached ribs due to small clearance between the rib and impingement surface. It can be observed that the stagnation point Nu for flat plate is higher compared to detached rib and for the detached rib the maximum Nu is shifted towards the rib clearance (Fig. 10). The reason behind the decreased stagnation point Nu for the detached rib is the rib projection or blockage and the formation of air bubble near the stagnation region. If the jet intensity is not strong enough to penetrate this air bubble formed, the stagnation point Nu will be lower than that in the case of flat plate. However, if the jet containing larger turbulence can hit the target surface or for small air bubble formation, e.g., with more clearance between the rib and impingement surface or the location of first rib changes, then an augmentation in the stagnation point Nu can be achieved. With this aim, we have investigated the detached rib configuration with different clearances ($c/B = 0, 0.135$ and 0.201) and the location of the first rib with $x/B(R_1) = 1$.

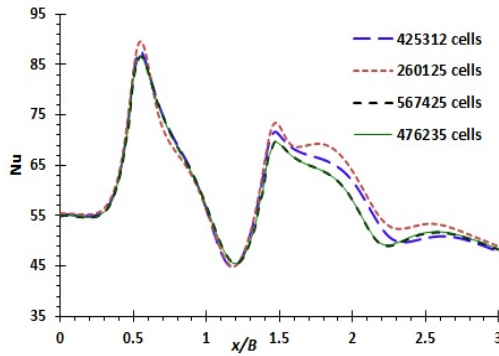


Fig. 9. Grid independence study for detached rib with Nu prediction at $H/B = 4$, $c/B = 0.067$, $x/B (R_1) = 0.5$, $p/e = 4$ and $Re = 20000$.

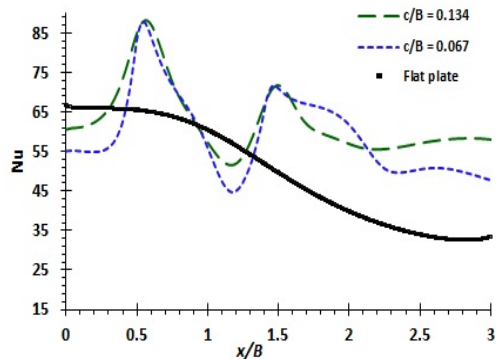


Fig. 10. Comparison of local Nu for flat and detached ribs at $H/B = 4$, $x/B (R_1) = 0.5$, $p/e = 4$, $Re = 20000$ for different c/B values.

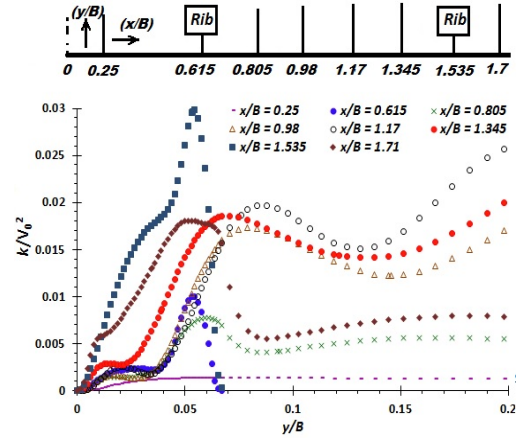


Fig. 11. Distribution of TKE (k) at different x/B values along y/B for detached rib at $H/B = 4$, $c/B = 0.067$, $x/B (R_1) = 0.5$, $p/e = 4$ and $Re = 20000$.

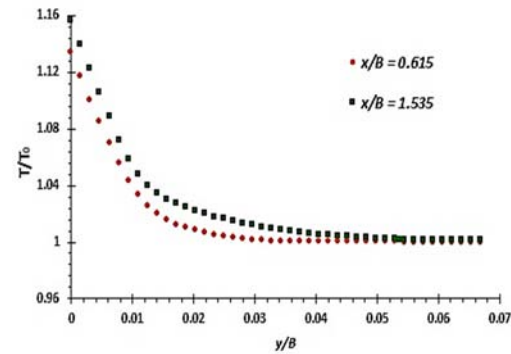


Fig. 12. Distribution of normalized temperature at $x/B = 0.615$ and 1.535 near detached rib surface at $H/B = 4$, $c/B = 0.067$, $x/B (R_1) = 0.5$, $p/e = 4$ and $Re = 20000$.

Figure 11 shows profiles of normalized TKE at different x/B locations near the impingement surface. All the x/B locations were selected so that the flow characteristics in the vicinity of the stagnation region and detached ribs can be obtained (values of $x/B = 0.615$ and 1.535 represent locations of the clearance between the rib and impingement surface). Values of TKE are higher in the region of the second rib clearance, i.e., at $x/B = 1.535$ and near the second rib (Fig. 11). It can also be observed that the flow acceleration starts in the first rib clearance where an augmentation in the value of TKE can be seen at $x/B = 0.615$ compared to $x/B = 0.25$ (Fig. 11). Thus the value of Nu increases in the region of rib clearance (Fig. 9). Heat transfer shows the maximum value at the location of the first rib clearance than at the second rib clearance. The primary reason for the local heat transfer to be maximum at the first rib clearance compared to the second one is due to a difference in flow temperatures (Fig. 12). Impinging jet flow is cold at the first rib location compared to the second rib location (Fig. 12).

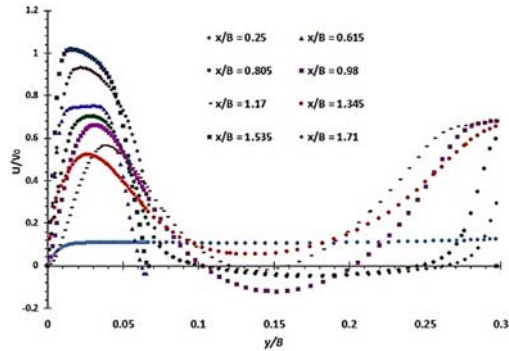


Fig. 13. Profiles of normalized streamwise velocity at different x/B locations along y/B for detached rib at $H/B = 4$, $c/B = 0.067$, $x/B (R_1) = 0.5$, $p/e = 4$ and $Re = 20000$.

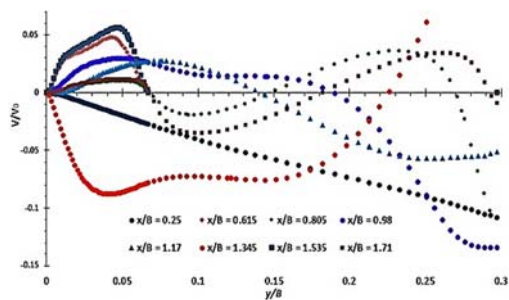


Fig. 14. Profiles of normalized normal velocity at different x/B locations along y/B for detached rib at $H/B = 4$, $c/B = 0.067$, $x/B (R_1) = 0.5$, $p/e = 4$ and $Re = 20000$.

Figures 13 and 14 show normalized x and y -velocities at different x/B locations close to the heated ribbed surface. Due to the clearance between the rib and surface the flow acceleration takes place at the locations of rib clearance, i.e., at $x/B = 0.615$ and 1.535 (Fig. 13). The normalized streamwise velocity attains higher values in the clearance of the second rib compared to the first rib clearance, but in both the cases the values were found to be the largest compared to the upstream and downstream values at the corresponding rib positions (Fig. 13). By virtue of the flow acceleration in the rib clearances, heat transfer attains higher values compared to the other regions. It can be observed from Fig. 14 that the vertical velocity decreases in the rib clearance due to flow acceleration in the x -direction. Flow recirculations can be observed in Figs. 13 and 14. Flow acceleration in the streamwise velocity can be related to a decrease in the vertical velocity at the corresponding regions.

Figure 15 shows a comparison of the stagnation point Nu for flat, detached and attached rib surfaces at $H/B = 4$, $x/B (R_1) = 0.5$, $p/e = 4$, $Re = 20000$ at different c/B values. It can be observed that the stagnation point Nu is more for the flat plate case than that for the ribbed case with $c/B = 0$, 0.067 and 0.134 except $c/B = 0.201$ (here $c/B = 0$ represents the attached rib configuration). With an increase in the clearance between the rib and impingement surface ($c/B = 0.201$), the stagnation point Nu is found to be more

than that for the flat plate. This behavior is because more fluid impinges on the surface as the blockage is reduced by increasing the clearance between the rib and surface.

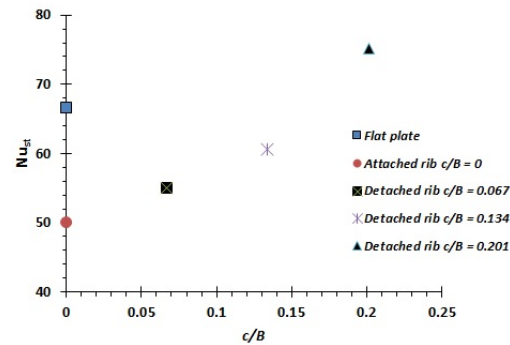


Fig. 15. Comparison of stagnation point Nusselt number (Nu_{st}) for flat, detached and attached rib surfaces at $H/B = 4$, $x/B (R_1) = 0.5$, $p/e = 4$, $Re = 20000$ at different c/B values.

The effect of the location of the first rib [with $x/B(R_1) = 0.5$ and 1] on the local Nusselt number is also presented in Fig. 16. Here the local Nusselt number distribution in the streamwise direction is found to be more with the placement of the first rib at $x/B(R_1) = 1$ than the smaller one. It can also be observed that the stagnation point Nu increases with the location of the first rib (Fig. 16). This behavior can be attributed to the fact that more fluid can actively impinge on the plate with an increase in the position of the first rib. A reduction in the horizontal momentum of impinging jet due to the rib placement is small with $x/B (R_1) = 1$ than that with $x/B (R_1) = 0.5$ (near the stagnation region). Table 2 shows a comparison of the normalized average Nu for different configurations up to $x/B = 3$. Here the average Nu is normalized with the stagnation point Nu of the flat plate. It can be observed that the average Nu for the detached rib configuration is more than that for flat plate and attached rib configurations (Table 2). In the case of the detached rib, if the location of the first rib increases from $x/B(R_1) = 0.5$ to 1 the average Nu increases approximately by 18.18%.

Table 2 Comparison of average Nu for different cases considered in the present study

S. No.	Configurations	Re	Nu_{av}/Nu_{st}
1.	Flat plate ($H/B = 4$)	20000	0.84
2.	Detached rib [$H/B = 4$, $c/B = 0.067$, $x/B(R_1) = 0.5$]	20000	0.88
3.	Detached rib [$H/B = 4$, $c/B = 0.067$, $x/B(R_1) = 1$]	20000	1.04
4.	Attached rib [$H/B = 4$, $c/B = 0$, $x/B(R_1) = 0.5$]	20000	0.81

Effect of Re on the local Nu is also considered for detached rib with $H/B = 4$, $x/B (R_1) = 0.5$, $c/B = 0.067$

and $p/e = 4$ (Fig. 17). An increase in Re has a favorable result on spread of the local Nu in the streamwise direction and therefore an enhancement in heat transfer can be achieved by increasing Re . Additionally the stagnation point Nu also increases with Re . This is due to the fact that with increasing Re the impinging jet can hit the target surface containing more turbulence and hence the colder fluid can penetrate the air bubble formed between and around the rib projections. Further the horizontal momentum of jet also increases with Re .

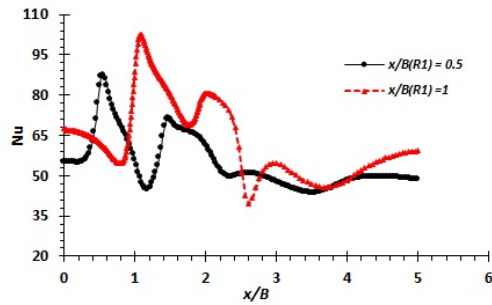


Fig. 16. Comparison of local Nu for detached rib surface for $H/B = 4$, $x/B (R_1) = 0.5$ and 1 , $p/e=4$, $c/B = 0.0067$ at $Re = 20000$.

Figure 18 shows the effect of the detachment of rib from the target surface by considering the attached and detached rib configurations. It can be observed here that the detached rib configuration offers an augmentation in Nu compared to the attached rib arrangement. The local Nu increases with detached rib configuration especially in the region of the rib clearance, due to a sudden flow acceleration (Fig. 18). On the other hand, in the case of the attached rib configuration (i.e., $c/B = 0$) the distribution of local Nu shows the opposite trend (a decreased value in the vicinity of the rib than that in the detached rib case). This behavior is due to the clearance which offers less resistance to the wall jet flow than the attached rib and therefore decrease in the horizontal momentum of the wall jet is large with the attached rib.

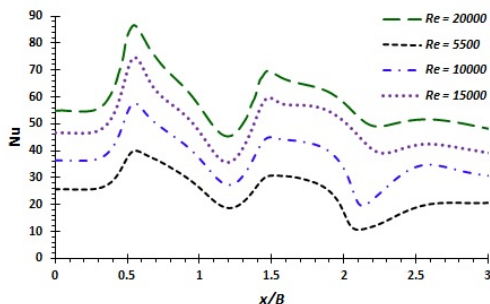


Fig. 17. Effect of Re on local Nu for detached rib surface at $H/B = 4$, $x/B (R_1) = 0.5$, $p/e = 4$ and $c/B=0.067$.

In the case of the attached rib, flow separation, recirculation and reattachment take place due to the

presence of rib. In the case of jet impingement the flow is not strong enough to penetrate air bubble formed (or recirculation region) and hence flow does not effectively impinge on the surface. Due to this behaviour, the heat transfer decreases compared to the detached rib configuration. With the detached rib configuration the heat transfer locally deteriorates between the ribs because counter-rotating vortices are formed after the detached ribs [Fig. 18(b)] and impinging jet cannot penetrate these effectively.

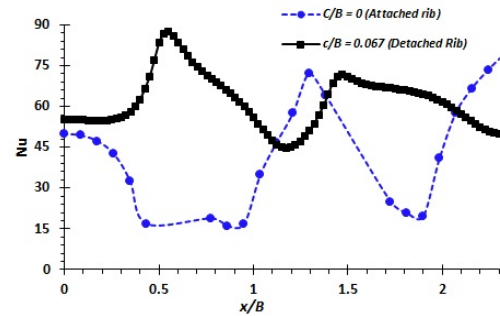


Fig. 18. Comparison of local Nu for detached ($c/B = 0.067$) and attached rib ($c/B = 0$) surfaces with $H/B=4$, $x/B (R_1)=0.5$, $p/e=4$ at $Re=20000$.

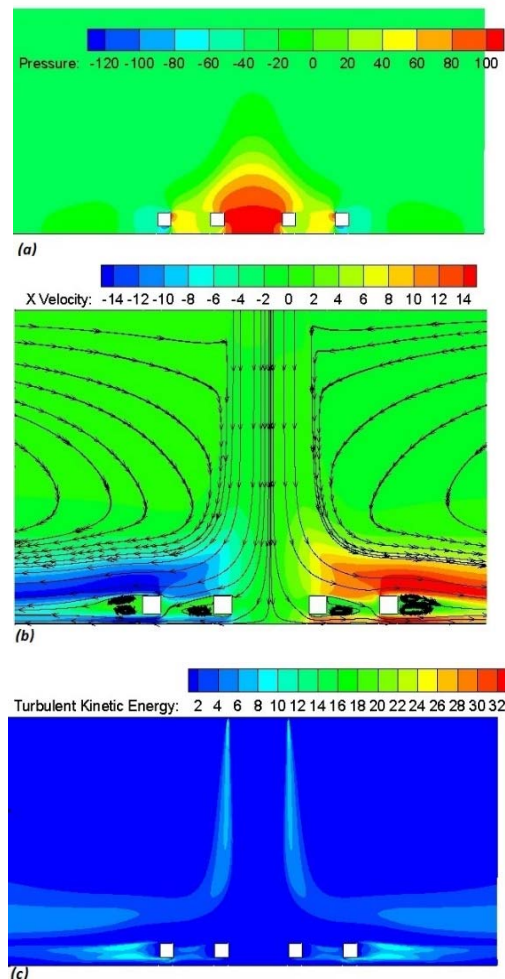


Fig. 19. (a, b, c) Contours of pressure, streamwise velocity and turbulent kinetic energy for detached rib at $H/B=4$.

Figure 19 shows contours of pressure, streamwise velocity and *TKE* for the detached rib configuration. It can be observed that the pressure is higher in the stagnation region and between the detached ribs [Fig. 19(a)]. The accelerated flow in the clearance between the rib and surface can be seen and the velocity is reduced to zero at the stagnation point [Fig. 19(b)]. The flow stagnation can be observed immediately before each rib and counter-rotating vortices can also be observed immediately after the detached ribs [Fig. 19(b)]. Contours of *TKE* show increased level in the clearances and after the second rib [Fig. 19(c)]. It can be noticed from Figs. 7 and 19 that the flow patterns are different with the detached rib surface than with the flat surface. We have also observed significant change in heat transfer behavior with the use of detached rib compared to the flat plate.

4. CONCLUSION

A computational study of slot jet impingement over flat and detached ribbed surfaces has been performed. Five RANS based turbulence models, all three variants of *k-ε* model (standard, RNG and realizable) and two *k-ω* based model (standard *k-ω* model and SST *k-ω* model) were considered. Some turbulence models predicted the experimental data with good trends, e.g., secondary peak in Nusselt number and distribution of normalized streamwise velocity. It was observed that the standard *k-ω* and SST *k-ω* models predict heat transfer more accurately than that by the variants of the *k-ε* turbulence model. Turbulent kinetic energy and streamwise and normal velocities close to the impingement surface were also analyzed in order to understand the heat transfer behavior with flat and detached rib surfaces. Further the effect of rib to plate clearance, position of first rib and Reynolds number on the heat transfer characteristics were investigated. It was observed that there is a significant effect of the placement of ribs on the impingement surface. Increasing rib clearance, position of first rib in the streamwise direction and Reynolds number have favorable effects on heat transfer. Comparisons of stagnation point and average Nusselt numbers are also presented to gain a good understanding of heat transfer enhancement with ribbed surfaces compared to a flat surface. The detached rib configuration offered augmentation in Nusselt number compared to the attached rib arrangement. With the detached rib configuration the heat transfer deteriorated locally between ribs due to the formation of counter-rotating vortices and impinging jet did not penetrate it effectively. However, heat transfer enhancement occurred in the clearances between the rib and surface due to the flow acceleration. It was also observed that the flow and heat transfer performances were different with the ribbed surfaces compared to the flat plate. The findings of the present paper will be useful industrial applications of jet impingement heat transfer, such as, cooling of electronic chips, turbine blades and combustor wall, etc.

ACKNOWLEDGEMENTS

The reported study is a part of the Department of

Science and Technology (DST), Government of India, New Delhi, sponsored project (SR/S3/MERC/0114/2012). Authors acknowledge the financial support received from DST.

REFERENCES

- Al-Sanea, S. (1992). A numerical study of the flow and heat transfer characteristics of an impinging laminar slot-jet including crossflow effects. *International journal of Heat and Mass Transfer* 35(10), 2501-2513.
- Arquis, E., M. A. Rady and S. A. Nada (2007). A numerical investigation and parametric study of cooling an array of multiple protruding heat sources by a laminar slot air jet. *International journal of Heat and Fluid Flow*, 28(4), 787-805.
- Ashforth Frost, S. and K. Jambunathan (1996). Effect of nozzle geometry and semi-confinement on the potential core of a turbulent axisymmetric free jet. *International Communications in Heat and Mass Transfer*, 23(2), 155-162.
- Ashforth Frost, S., K. Jambunathan and C. F. Whitney (1997). Velocity and turbulence characteristics of a semiconfined orthogonally impinging slot jet. *Experimental Thermal and Fluid Science* 14(1), 60-67.
- Behnia, M., S. Parneix, Y. Shabany and P. A. Durbin (1999). Numerical study of turbulent heat transfer in confined and unconfined impinging jets. *International Journal of Heat and Fluid Flow*, 20(1), 1-9.
- Buchlin, J. M. (2011). Convective heat transfer in impinging-gas-jet arrangements *Journal of Applied Fluid Mechanics* 4(2), 137-149.
- Charmiyan, M., A. R. Azimian, L. Keirsbulc, E. Shirani and F. Aloui (2016). Turbulent Plane Impinging Jet-Physical Insight and Turbulence Modeling. *Journal of Applied Fluid Mechanics*, 9(1), 11-17.
- Cziesla, T., G. Biswas, H. Chattopadhyay and N. K. Mitra (2001). Large-eddy simulation of flow and heat transfer in an impinging slot jet. *International Journal of Heat and Fluid Flow*, 22(5), 500-508.
- Dairay, T., V. Fortuné, E. Lamballais, and L. E. Brizzi (2014). LES of a turbulent jet impinging on a heated wall using high-order numerical schemes. *International Journal of Heat and Fluid Flow*, 50, 177-187.
- Dewan, A. (2011). *Tackling turbulent flows in engineering*. Springer Science and Business Media.
- Dewan, A., R. Dutta and B. Srinivasan (2012). Recent trends in computation of turbulent jet impingement heat transfer. *Heat Transfer Engineering* 33(4-5), 447-460.
- Dutta, R., A. Dewan and B. Srinivasan (2013). Comparison of various integration to wall

- (ITW) RANS models for predicting turbulent slot jet impingement heat transfer. *International Journal of Heat and Mass Transfer* 65, 750-764.
- Dutta, R., A. Dewan and B. Srinivasan (2016). Large Eddy Simulation of Turbulent Slot Jet Impingement Heat Transfer at Small Nozzle-to-Plate Spacing. *Heat Transfer Engineering* 37(15), 1242-1251.
- Dutta, R., B. Srinivasan and A. Dewan (2013b). LES of a Turbulent Slot Impinging Jet to Predict Fluid Flow and Heat Transfer. *Numerical Heat Transfer, Part A: Applications* 64(10), 759-776.
- Gau, C. and C. C. Lee (1992). Impingement cooling flow structure and heat transfer along rib-roughened walls. *International Journal of Heat and Mass Transfer* 35(11), 3009-3020.
- Gau, C. and I. C. Lee (2000). Flow and impingement cooling heat transfer along triangular rib-roughened walls. *International Journal of Heat and Mass Transfer* 43(24), 4405-4418.
- Hoogendoorn, C. J. (1977). The effect of turbulence on heat transfer at a stagnation point. *International Journal of Heat and Mass Transfer* 20(12), 1333-1338.
- Katti, V. and S. V. Prabhu (2008). Heat transfer enhancement on a flat surface with axisymmetric detached ribs by normal impingement of circular air jet. *International Journal of Heat and Fluid Flow*, 29(5), 1279-1294.
- Kedar, B., (1981). Temperature and Concentration Profiles in Fully Turbulent Boundary Layers. *International Journal of Heat and Mass Transfer* 24(9), 1541-1544.
- Krishnamurthy, M. R., B. J. Gireesha, B. C. Prasannakumara and R. S. R. Gorla (2016). Thermal radiation and chemical reaction effects on boundary layer slip flow and melting heat transfer of nanofluid induced by a nonlinear stretching sheet. *Nonlinear Engineering*, 5(3), 147-159.
- Lauder, B. E. and D. B. Spalding (1974). The numerical computation of turbulent flows, *Computer Methods in Applied Mechanics and Engineering* 3, 269-289.
- Livingood, J. N. and P. Hrycak (1973). Impingement heat transfer from turbulent air jets to flat plates: a literature survey, NASA TM X-2778.
- Lytle, D. and B. W. Webb (1994). Air jet impingement heat transfer at low nozzle-plate spacings. *International Journal of Heat and Mass Transfer* 37(12), 1687-1697.
- Menter, F. R. (1994). Two-equation eddy-viscosity turbulence models for engineering applications. *AIAA journal*, 32, 1598-1605.
- Investigation of a Confined Laminar Slot Jet on a Solid Block. *Journal of Applied Fluid Mechanics* 9(4).
- O'Donovan, T. S. and D. B. Murray (2007). Jet impingement heat transfer—Part II: A temporal investigation of heat transfer and local fluid velocities. *International Journal of Heat and Mass Transfer* 50(17), 3302-3314.
- Ramesh, G. K., B. C. Prasannakumara, B. J. Gireesha and M. M. Rashidi (2016). Casson Fluid Flow near the Stagnation Point over a Stretching Sheet with Variable Thickness and Radiation. *Journal of Applied Fluid Mechanics*, 9 (3), 1115-1122.
- Ramesh, G. K., B. J. Gireesha and R. S. R. Gorla (2015). Boundary layer flow past a stretching sheet with fluid-particle suspension and convective boundary condition. *Heat and Mass Transfer* 51, 1061-1066.
- Shih, T. H., W. W. Liou, A. Shabbir, Z. Yang and J. Zhu (1995). A new $k-\epsilon$ eddy viscosity model for high Reynolds number turbulent flows - model development and validation, *Computers and Fluids* 24, 227-238.
- Shukla, A. K. and A. Dewan (2016). Computational study on effects of rib height and thickness on heat transfer enhancement in a rib roughened square channel. *Sādhanā - Academy Proc. In Engineering Science* 41(6), 667-678.
- Shukla, A. K. and A. Dewan (2017). Flow and thermal characteristics of jet impingement: comprehensive review. *International Journal of Heat and Technology*, 35(1), 153-166.
- Tan, L., J. Z. Zhang and H. S. Xu (2014). Jet impingement on a rib-roughened wall inside semi-confined channel. *International Journal of Thermal Sciences* 86, 210-218.
- Wilcox, D. C. (2006). Turbulence modeling for CFD, *La Canada*, California, USA.
- Wolfstein, M., (1969). The Velocity and Temperature Distribution of One-Dimensional Flow with Turbulence Augmentation and Pressure Gradient. *International Journal of Heat and Mass Transfer*, 12, 301-318.
- Yakhot, V. and S. A. Orszag (1986). Renormalization group analysis of turbulence: I. basic theory, *Journal of Scientific Computing* 1, 1-51.
- Zhe, J. and V. Modi (2001). Near wall measurements for a turbulent impinging slot jet (data bank contribution). *ASME Journal of Fluids Engineering* 123(1), 112-120.
- Zuckerman, N. and N. Lior (2006). Jet impingement heat transfer: physics, correlations, and modeling. *Advances in Heat Transfer* 31.